Available online at www.sciencedirect.com
ScienceDirect
Trans. Nonferrous Met. Soc. China 32(2022) 765−777
Transactions of Nonferrous Metals Society of China
www.tnmsc.cn

# Diversity of intergranular corrosion and stress corrosion cracking for 5083 Al alloy with different grain sizes

Jin QIN[1,2], Zhi LI[3], Ming-yang MA[1,2], Dan-qing YI[1,2], Bin WANG[1,2]

1. School of Materials Science and Engineering, Central South University, Changsha 410083, China;
2. Key Laboratory of Nonferrous Metal Materials Science and Engineering, Ministry of Education, Central South University, Changsha 410083, China;
3. The Second Research Institute of Civil Aviation Administration of China, Chengdu 610064, China

Received 15 April 2021; accepted 16 November 2021

**Abstract:** 5083 Al alloy sheets with different grain sizes (8.7−79.2 μm) were obtained by cold rolling and annealing. Their microstructures, intergranular corrosion (IGC), stress corrosion cracking (SCC), and crack propagation behaviors were investigated. The results showed that samples with coarse grains exhibit better IGC resistance with a corrosion depth of 15 μm. The slow strain rate test results revealed that fine-grained samples exhibit better SCC resistance with a susceptibility index ($I_{SSRT}$) of 11.2%. Furthermore, based on the crack propagation mechanism, grain refinement can improve the SCC resistance by increasing the number of grain boundaries to induce the corrosion crack propagation along a tortuous path. The grains with {011} orientation could hinder crack propagation by orientating it toward the low-angle grain boundary region. The crack in the fine-grained material slowly propagates due to the tortuous path, and low $H^+$ and $Cl^-$ concentrations.

**Key words:** grain size; intergranular corrosion; stress corrosion cracking; crack propagation; 5083 Al alloy

## 1 Introduction

With rapid development of the manufacturing and processing industry and intensified world energy shortage, the shipbuilding, automobile, rail traffic, and other industries require lightweight structural parts that satisfy the required strength. Particularly, 5083 Al alloy is widely used for its excellent welding performance and good corrosion resistance [1]. Owing to its anti-corrosive property, 5083 Al alloy is currently employed as a ship material that can mitigate intergranular corrosion (IGC) and stress corrosion cracking (SCC) for long-term exposure to seawater [2,3].

The IGC/SCC susceptibility of Al−Mg alloys is influenced by their microstructures, such as grain orientation, alloying elements, solution chemistry, grain size, precipitates, and heat-treatment methods. LI et al [4] reported that 5083 Al alloys dominated by brass grains exhibit the highest resistance to SCC with a stress corrosion susceptibility index ($I_{SSRT}$) of 11.7%. MENG et al [5] suggested that the SCC resistance of an Al−Mg alloy is significantly improved by Zn addition in an acidified NaCl solution; SCC susceptibility was nearly eliminated when the Zn content was 1.0%. ZHAO et al [6] reported that the addition of Zn improves the corrosion resistance of an Al−Mg alloy, finding the optimal amount to be 0.31% Zn, which precluded the precipitation of the $\beta$-phase ($Al_3Mg_2$) at the grain boundary (GB). FAN et al [7] noted grain refinement as an effective approach to enhancing strength and SCC resistance, suggesting that the Mg/Si ratio could be used as a critical indicator for the development of novel, advanced, corrosion-

**Corresponding author:** Bin WANG, Tel: +86-731-88836320, E-mail: wangbin325@263.net
DOI: 10.1016/S1003-6326(22)65831-X
1003-6326/© 2022 The Nonferrous Metals Society of China. Published by Elsevier Ltd & Science Press

resistant Al−Mg alloys. DING et al [8] showed that when the annealing temperature was changed from 200 to 220 °C, the 5083 Al alloy transformed from a sensitized to stabilized state, corresponding to the change in the nucleation position of $\beta$ precipitates from GBs to triple junctions. MA et al [9] demonstrated that the good corrosion resistance of Al−Mg alloys retrogressed at 405 and 420 °C.

Grain size variations are known to affect GB density of an alloy, as well as GB size and angle ratio, thereby affecting its SCC performance [10]. The literature includes contradicting results on the influence of grain size on SCC behavior. HUANG et al [11] succeeded in increasing the GB area of an AZ80 Mg alloy through grain refinement which was achieved by reducing the mismatch between the passivation film and metal matrix and enhancing the cohesion of the interface, thereby improving the stress corrosion resistance of the alloy. SUN et al [12] demonstrated the coarse-grain area of the surface layer of an LY12 Al alloy as an effective corrosion barrier that could slow down the IGC rate, thereby reducing the stress corrosion resistance of the alloy. TSAI and CHUANG [13] found that a fine-grained 7475 Al alloy sheet has better stress-corrosion resistance that can be attributed to its grain refinement, leading to a more uniform sliding mode and smaller GB precipitates. In addition, the coarse grains were found to improve the SCC performance of the alloy. AEGADE et al [14] studied the SCC behavior of coarse, fine, and ultra-fine-grained Al−Mg−Sc−Zr alloys. They found that ultra-fine-grained Al−4Mg−0.8Sc−0.08Zr is extremely sensitive to SCC, having an $I_{SSRT}$ of 55%. The high GB area per unit volume in the ultra-fine grains makes it easier for hydrogen to diffuse in the matrix, promoting its sensitivity to SCC. OSÓRIO et al [15] reported the improved corrosion resistance of the coarse-grained, relative to fine-grained, columnar and equiaxed structures in Al castings. These findings were similar to those obtained by MAHMOUD [16].

For corrosion-resistant 5083 Al alloy, the influence of the grain size on the SCC sensitivity has not been systematically studied. Owing to its wide applications in the transportation industry, it is imperative to investigate the corrosion resistance of 5083 Al alloy. In this study, the effect of grain sizes on the susceptibility of this alloy to SCC was assessed. The IGC test, slow strain rate test (SSRT), and electron back-scattered diffraction (EBSD) were used to compare the corrosion and SCC behavior of 5083 Al alloy plates with different grain sizes, revealing their related mechanisms on SCC behavior. Based on the relationship between SCC and grain size, better performance can be produced in the manufacturing process of 5083 Al alloy.

## 2 Experimental

### 2.1 Material preparation

A 12.0 mm cold-rolled 5083 Al sheet, provided by Henan Mingtai Aluminum Co., Ltd. (China), was used in this study. It had a nominal composition of 4.38 wt.% Mg, 0.64 wt.% Mn, 0.25 wt.% Si, and 0.27 wt.% Fe, with the balance Al. To prepare samples with different grain sizes, the 5083 Al sheet was cold rolled to different thicknesses with the rolling reduction rates of 5%, 8%, 10%, 15%, 25%, 50%, and 75%, respectively.

The cold-rolled sheets were then annealed at 400 °C for 1 h. Subsequently, the samples were annealed at 170 °C for 24 h to eliminate internal stress (sensitization) without affecting the grain size. To prove that recrystallization occurred at 400 °C and that the annealing at 170 °C did not affect the grain size, Fig. 1 shows the Vickers hardness of the 5083 Al alloy obtained at different annealing temperatures. The cold-rolled sheets were annealed at different temperatures from 200 to 290 °C, resulting in various levels of recovery/partial recrystallization and the Vickers hardness values in the range of HV 75−110. The significant drop in hardness at 250 °C can be attributed to the primary

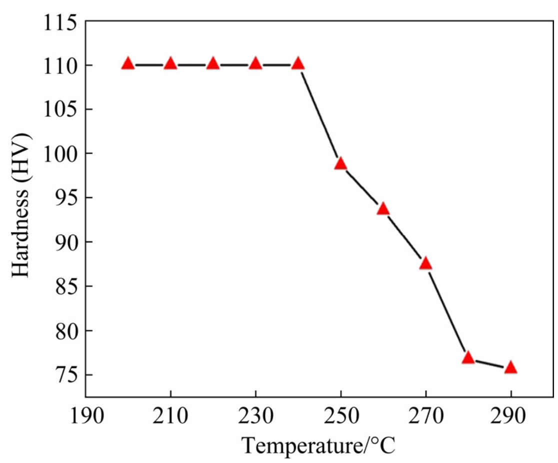


**Fig. 1** Evolution of Vickers hardness of 5083 Al alloys during annealing at different temperatures [4]

recrystallization process, which can reduce the dislocation density [17,18]. This implies that recrystallization occurred at annealing temperature of 250 °C and higher. Moreover, to determine the effect of the grain size on the SCC performance of the 5083 Al alloy, four samples with grain sizes of 8.7 μm (Sample 1), 24.4 μm (Sample 2), 43.7 μm (Sample 3), and 79.2 μm (Sample 4) were produced.

### 2.2 IGC and electrochemical performance

The samples were ground, polished, and then immersed in concentrated nitric acid at 30 °C for 24 h. The IGC resistance of four samples was assessed using a nitric acid mass loss test (NAMLT) following ASTM G67−04. The cross-sectional depth of the polished and corroded sample was measured under an optical microscope to assess the intergranular damage. A potentiodynamic polarization test was performed on a CS2350 electrochemical workstation. To obtain the appropriate polarization interval, the working electrode was placed in a 3.5 wt.% NaCl solution at 25 °C for 0.5 h before the test. The electrode polarization was conducted at a potential interval of ±0.6 V and scanning speed of 1 mV/s. To ensure reproducibility, all electrochemical measurements were performed at least three times.

### 2.3 SSRT

SSRT was carried out on a slow strain rate tensile test machine (YYF−50) to analyze the SCC behavior of the samples. After mounting the tensile test specimen on the machine, a stress of approximately 100 N was preloaded and the strain rate was set to be $1.0\times10^{-6}$ s$^{-1}$. The experiment was then carried out in air and 3.5 wt.% NaCl solution. The test was repeated thrice for each sample. All specimens were abraded along the tensile direction using 400, 600, and 800 grit abrasive papers, and dried in cool air. After cleaning away the corrosion products, the fracture surfaces of the SSRT samples were observed by scanning electron microscopy (SEM). The relative plastic loss ($I_\delta$) of the sample obtained after testing in air and NaCl solution was used to evaluate the SCC susceptibility, as shown in Eq. (1) [19]:

$$I_\delta = (1-\frac{\delta_{\mathrm{sol}}}{\delta_{\mathrm{air}}})\times 100\% \tag{1}$$

where $\delta_{\mathrm{air}}$ and $\delta_{\mathrm{sol}}$ are the elongations in air and the solution, respectively.

### 2.4 Microstructural characterization

The morphological characteristics of the prepared samples were characterized by optical microscopy (POLYVER-MET), SEM (Quanta−200 and FEI-Sirion−200), and EBSD. The 400#, 600#, 800# sandpapers were used to grind the samples, then the samples are polished by 60 nm $SiO_2$ suspension to obtain a smooth surface without scratches. The sample was then etched with a Barker reagent ($HBF_4$:$H_2O$=5:195) at 20 V for 5 min. The metallographic structure was observed under polarized light conditions. At least three photos were selected using Image J for each sample. Prior to the EBSD test, the specimens underwent electrolytic polishing in a mixture of 90 vol.% ethanol and 10 vol.% perchloric acid at a polishing voltage and temperature of 25 V and −20 °C, respectively. The EBSD data were analyzed using Channel 5 analysis software. After performing SSRT, the crack propagation path of the samples with different grain sizes was traced using SEM and EBSD.

## 3 Results and discussion

### 3.1 Microstructure

The metallographic structure of the alloy after annealing is shown in Fig. 2. Figure 2(i) presents a schematic diagram of the sample, showing the rolling direction (RD) and transverse direction (TD). The grains are well defined and elongated parallel to the RD. There are obvious differences in the grain characteristics of the 5083 Al alloy depending on the RD. For example, small equiaxed grains occur in Fig. 2(h). Using Image J software, the average grain sizes of all the samples are determined to be 23.5, 30.3, 44.2, 79.2, 59.6, 43.7, 24.4, and 8.7 μm for rolling reduction rates of 0%, 5%, 8%, 10%, 15%, 25%, 50%, and 75%, respectively. The grain sizes of the alloys are listed in Table 1.

The relationship between the rolling reduction rate and grain size of the 5083 Al alloy after recrystallization is shown in Fig. 3. As the rolling reduction rate increases from 0% to 10%, the grain size of the alloy sharply increases, reaching a maximum of 79.2 μm at a rolling reduction rate of

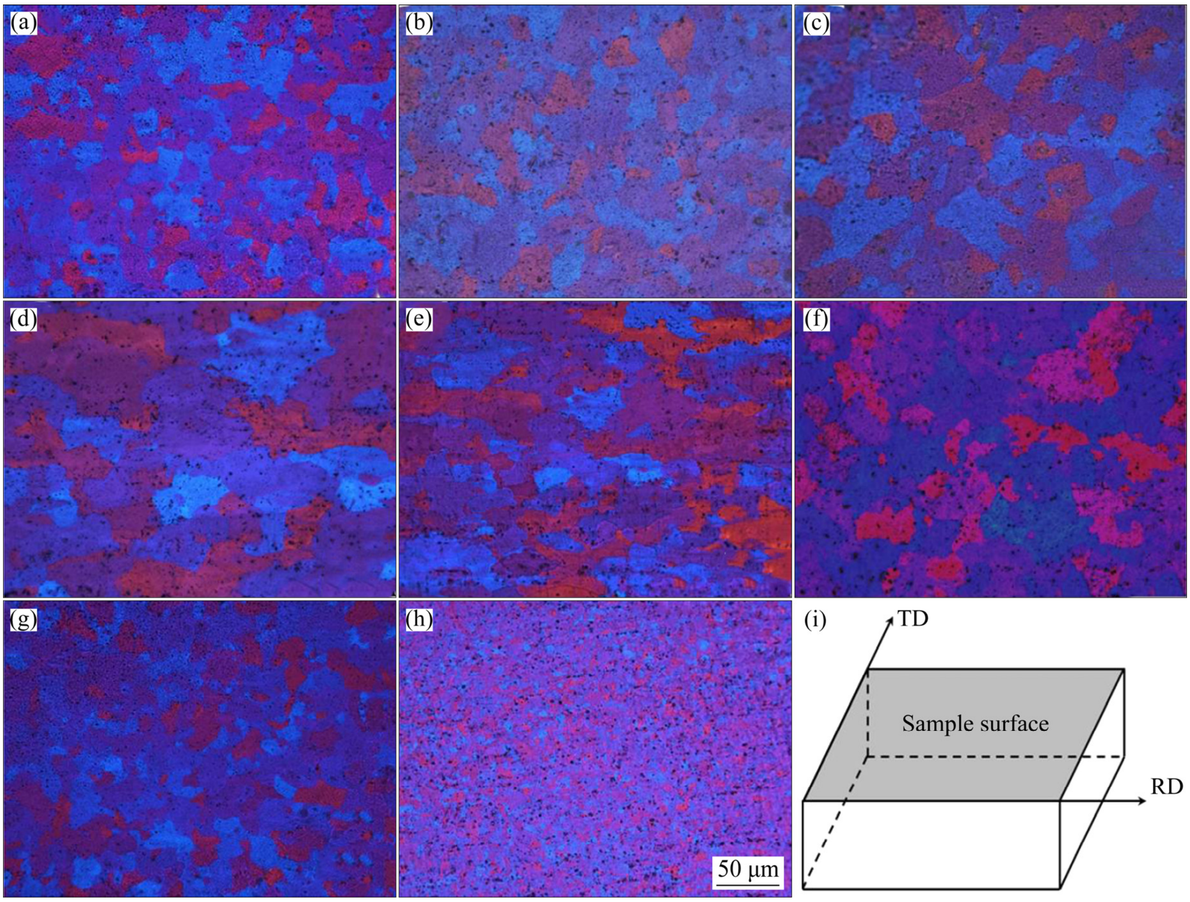


**Fig. 2** Metallographic structures of 5083 Al alloy after annealing with different rolling reduction rates: (a) 0%; (b) 5%; (c) 8%; (d) 10%; (e) 15%; (f) 25%; (g) 50%; (h) 75%; (i) Schematic diagram of sample

**Table 1** Grain sizes of 5083 Al alloy at different rolling reduction rates

| Rolling reduction rate/% | 0 | 5 | 8 | 10 | 15 | 25 | 50 | 75 |
|---|---|---|---|---|---|---|---|---|
| Grain size/ μm | 23.5 | 30.3 | 44.2 | 79.2 | 59.6 | 43.7 | 24.4 | 8.7 |

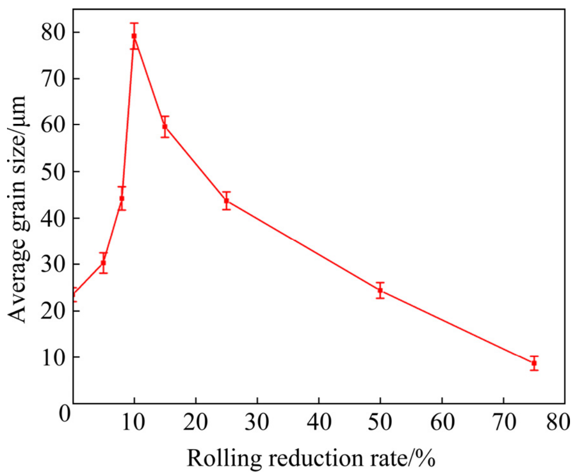


**Fig. 3** Relationship between rolling reduction rate and grain size of 5083 Al alloy after recrystallization

10%. As the rolling reduction rate further increases, the grain size gradually decreases. The grain size of a recrystallized Al alloy depends on the nucleation and subsequent growth rates where the driving force is provided by the stored deformation energy; therefore, a minimum deformation is required to initiate recrystallization [20,21]. Figure 3 shows that the low degree of deformation during the cold-rolling process releases sufficient stored energy to trigger recrystallization, resulting in the equiaxed shape of the grains. At a rolling reduction rate of 10%, energy stored in the alloy can cause initial recrystallization; this value is defined as the critical deformation degree; however, critical deformation increases the possibility of uneven deformation in the alloy, resulting in a low nucleation rate and producing coarse recrystallized grains. With the increase in the amount of deformation, the nucleation and growth rates of the recrystallized grains increase more rapidly, leading to a decrease in the grain size. SHOU et al [22] studied the grain size and microstructure of

2524-T3 Al alloy and they found that coarse recrystallized grains can be obtained through the combined effects of a low nucleation rate and high growth rate. Particularly, as the degree of deformation increases, the nucleation and growth rates of the recrystallized grains increase more quickly, resulting in the decrease in the grain size, which is consistent with the results obtained in this study.

The intermetallic inclusions in the 5083 Al alloy play a crucial role in determining its susceptibility to localized corrosion. Figures 4(a, b) show the SEM images of the intermetallic inclusions with their corresponding energy-dispersive spectroscopy (EDS) results. The white phase is elongated along the RD and distributed following a chain shape, whereas the gray phase is dispersed in the crystal. According to the results of previous studies, the white inclusion particles are $Al_6(Mn,Fe)$ phases, whereas the gray area is $Mg_2Si$ [23]. ImagePro 10 was used to measure the area fractions of the $Al_6(Mn,Fe)$ and $Mg_2Si$ particles in the four samples, which are found to be 1.7%, 0.4%; 1.9%, 0.3%; 1.8%, 0.2%; and 1.7%, 0.2%, respectively. The distribution and number of intermetallic inclusions have minimal effect on the NAMLT results.

### 3.2 IGC behavior

Figure 5 shows the cross-sectional micro-structure of the four 5083 Al sheet samples after IGC. Localized corrosion occurs due to the loss of the bonding force among surface grains of Sample 1. The typical IGC morphology of Sample 1 is shown in Fig. 5(a), in which the largest corrosion depth of 36 μm is observed. Meanwhile, instead of a typical IGC morphology, Samples 2−4 exhibit pitting corrosion on the corrosion surface, as shown in Figs. 5(b−d), respectively. Moreover, Sample 4 has the smallest corrosion depth of 15 μm. This conforms to the increasing trend in the IGC resistance of the alloy with an increase in the grain size.

Generally, the different IGC behaviors of the 5083 Al alloys with different grain sizes may be attributed to the GB distribution and energy level. Therefore, EBSD analyses were performed on the samples with fine and coarse grains. The EBSD results for Samples 1 and 4 are shown in Fig. 6, which demonstrates that recrystallization occurs during the annealing process. Most of the GBs in the samples are high-angle grain boundaries (HAGBs) with misorientation angles greater than 15°, as shown in Fig. 6(c). However, the HAGB fraction of Sample 1 is 1.38 times greater than that of Sample 4. Meanwhile, the fractions of low-angle grain boundaries (LAGBs) in Samples 1 and 4 are 16.5% and 39.4%, respectively. According to previous studies, GB misorientation affects IGC [24]. Since HAGBs have a higher energy level [25], fine-grained Al alloys could develop more local galvanic coupling between the grain boundaries and interiors, resulting in enhanced kinetic corrosivity [26]. LIU and ADAMS [27]

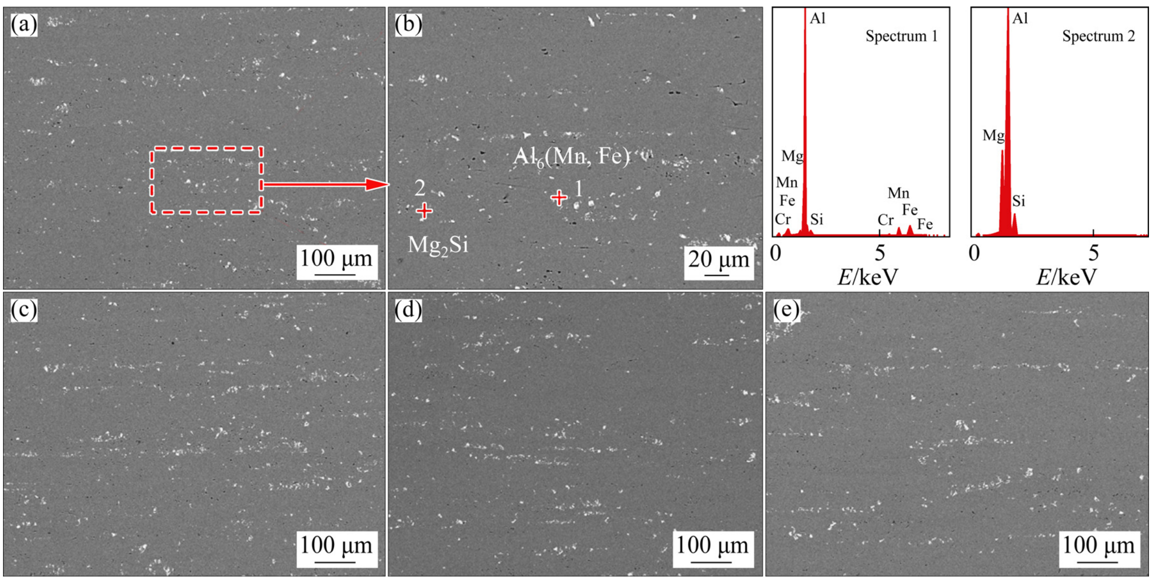


**Fig. 4** SEM images of intermetallic inclusions with corresponding EDS results: (a, b) Sample 1; (c) Sample 2; (d) Sample 3; (e) Sample 4

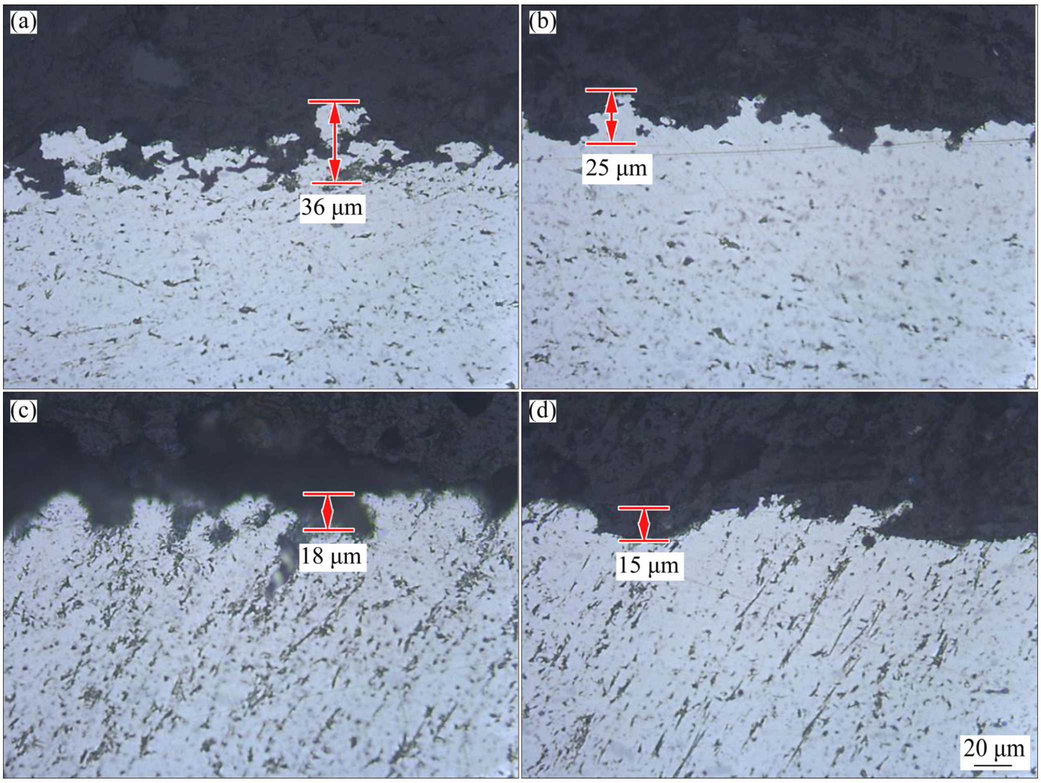


**Fig. 5** Optical microscopy images of samples after IGC: (a) Sample 1; (b) Sample 2; (c) Sample 3; (d) Sample 4

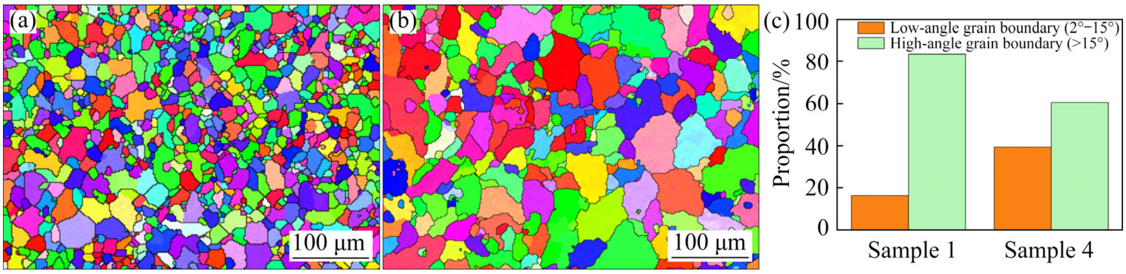


**Fig. 6** EBSD results for annealed samples: (a) Sample 1 [4]; (b) Sample 4; (c) GB misorientation distributions

carried out Monte-Carlo simulations to determine the degree of Mg enrichment at the GBs of Al−10%Mg alloys at high working temperatures. Grain refinement increases the GB density and micro-coupling. In addition, the GBs accelerate the diffusion and segregation of the atoms, and promote corrosion propagation [28,29]. In summary, IGC is more likely to occur on fine grains than on coarse grains.

A polarization curve is used to reveal the corrosion properties of an alloy. The polarization curves of the four samples obtained from the potential dynamic polarization test are shown in Fig. 7. The four samples exhibit similar polarization curves, indicating their similar polarization behavior. The corrosion potential ($\varphi_{corr}$) and corrosion current density ($J_{corr}$) derived from these

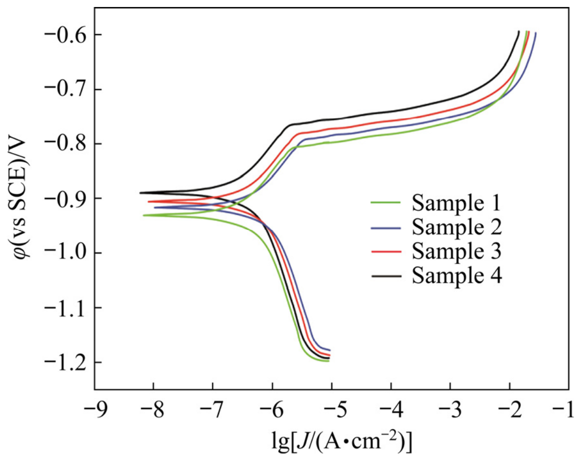


**Fig. 7** Polarization curves of 5083 Al samples

curves are listed in Table 3. Sample 1 has the smallest $\varphi_{corr}$ of −0.936 V, denoting that it is more prone to IGC. Moreover, it has the largest $J_{corr}$ of $6.4\times10^{-5}$ mA/cm$^2$, indicating that it has the fastest corrosion rate. In contrast, Sample 4 has the largest $\varphi_{corr}$ of −0.889 V, suggesting that it is less likely to experience IGC. Similarly, CUI et al [30] found that fine-grained samples have a more negative potential, higher chemical activity, and fast corrosion rate. This result is consistent with the polarization curve of Sample 1, which has fine grains, indicating its faster corrosion rate and higher susceptibility to IGC.

### 3.3 Slow strain rate test results

The typical stress−strain curves of the four samples in air and 3.5 wt.% NaCl solution were obtained from the SSRT, as shown in Fig. 8. The SCC susceptibilities of the samples were calculated according to Eq. (1). Their corresponding mechanical parameters are listed in Table 4. Sample 1 has the lowest SCC susceptibility with an $I_{SSRT}$ of 11.2%, indicating the best resistance to SCC among other samples. In contrast, Sample 4 exhibits the highest SCC susceptibility with an $I_{SSRT}$ of 40.5%, which is 72.3% higher than that of Sample 1, demonstrating the lowest resistance to SCC. Hence, samples with fine grains have better resistance to SCC than those with coarse grains. Moreover, the results in air show the relatively similar strength and elongation values for all samples. In contrast, there are clear differences noted on the elongation of the sample in NaCl solution. Sample 1 has the largest elongation of 21.4%, whereas Sample 4 has the smallest elongation of 13.2%. In addition, the elongation of the samples in NaCl solution is lower than that in air. This decrease in the elongation is attributed to the selective dissolution of the $\beta$-phase of the GB, which provides a path for IGC/IGSCC and causes the early fracture of the samples during SSRT in NaCl solution [31,32].

**Table 3** Polarization curve parameters of 5083 Al alloy samples

| Sample No. | $\varphi_{corr}$(vs SCE)/V | $J_{corr}$/(mA·cm$^{-2}$) |
|---|---|---|
| 1 | −0.936 | $6.4\times10^{-5}$ |
| 2 | −0.910 | $6.0\times10^{-5}$ |
| 3 | −0.905 | $6.1\times10^{-5}$ |
| 4 | −0.889 | $5.8\times10^{-5}$ |

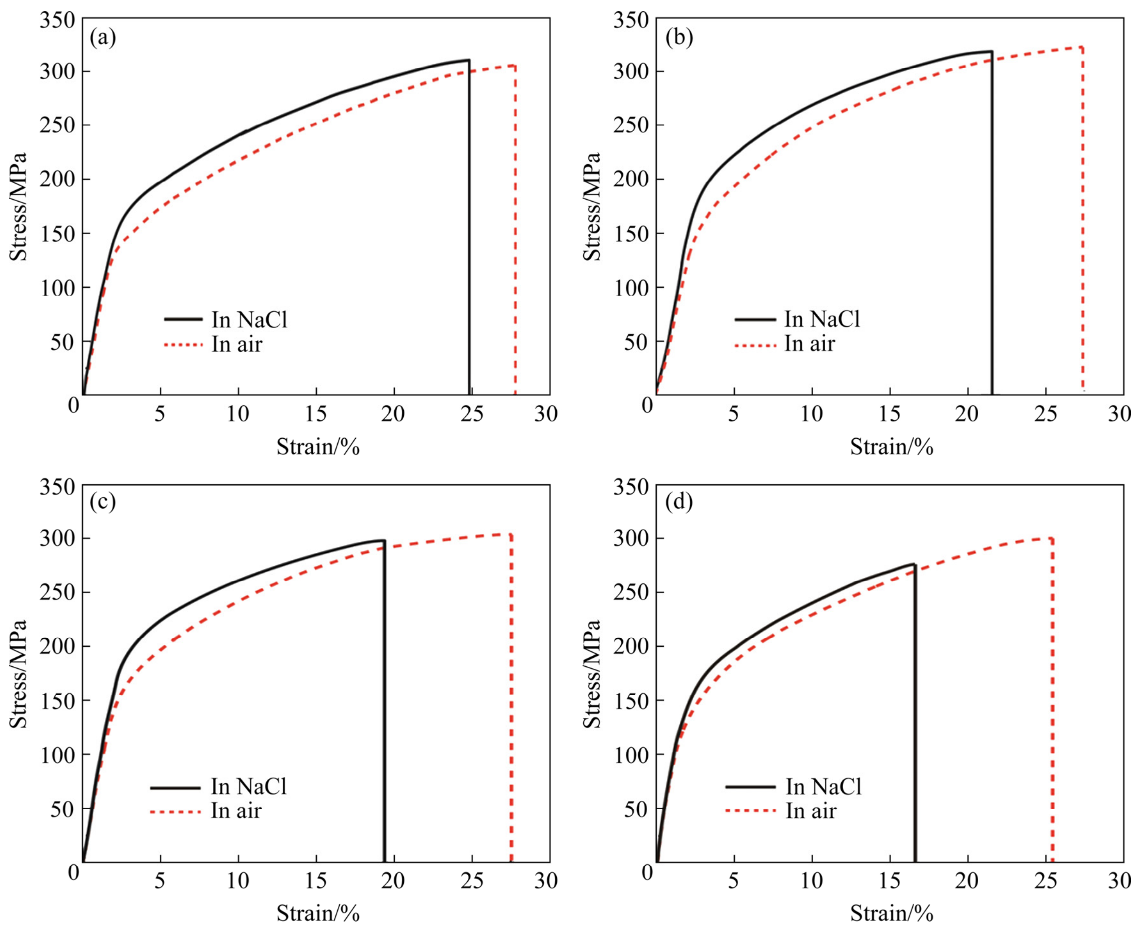


**Fig. 8** SSRT tensile curves in air and 3.5 wt.% NaCl solution: (a) Sample 1; (b) Sample 2; (c) Sample 3; (d) Sample 4

The SEM fracture morphologies of the 5083 Al alloy samples tested in a 3.5 wt.% NaCl solution are shown in Fig. 9. There are considerable variations in the fracture surfaces of the samples. For Sample 1, a significant number of large circular dimples caused by micro-void coalescence [33] are present over the majority of the fracture surface, as shown in Fig. 9(a). This further corresponds to the highest elongation of Sample 1 obtained by SSRT in 3.5 wt.% NaCl solution. In contrast, the fracture surfaces of Samples 2 and 3 have small flat areas with some dimples, as shown in Figs. 9(b, c). Meanwhile, Sample 4 has a nearly flat fracture surface, indicated by the dotted areas in Fig. 9(d). This can be attributed to brittle fracture, which is the representative feature of SCC. These brittle fracture features can be ascribed to the precipitation of the $\beta$-phase [34,35], which leads to pitting caused by anodic dissolution under corrosive conditions and consequently, accelerates fall-out of the particles due to SCC.

### 3.4 Crack propagation

The SCC behavior of an alloy results in a combination of tensile stress and corrosion and is usually related to crack formation and propagation.

**Table 4** Mechanical properties of 5083 Al alloys after SSRT

| Sample No. | In air | | | In 3.5 wt.% NaCl | | | $I_{SSRT}$/% |
|---|---|---|---|---|---|---|---|
| | UTS/MPa | YS/MPa | Elongation/% | UTS/MPa | YS/MPa | Elongation/% | |
| 1 | $307^{+3.2}_{-2.1}$ | $147^{+1.3}_{-0.8}$ | $24.1^{+0.5}_{-0.2}$ | $313^{+3.1}_{-1.9}$ | $170^{+1.3}_{-0.9}$ | $21.4^{+0.4}_{-0.3}$ | 11.2 |
| 2 | $325^{+2.3}_{-2.5}$ | $172^{+1.1}_{-0.7}$ | $22.7^{+0.6}_{-0.3}$ | $318^{+2.4}_{-2.1}$ | $203^{+1.2}_{-0.7}$ | $18.2^{+0.5}_{-0.2}$ | 19.8 |
| 3 | $308^{+1.8}_{-1.1}$ | $166^{+0.8}_{-0.5}$ | $23.1^{+0.7}_{-0.2}$ | $298^{+1.9}_{-1.6}$ | $197^{+0.9}_{-1.1}$ | $15.6^{+0.4}_{-0.4}$ | 32.5 |
| 4 | $301^{+2.7}_{-2.4}$ | $151^{+0.6}_{-1.1}$ | $22.2^{+0.8}_{-0.4}$ | $276^{+2.1}_{-1.3}$ | $167^{+1.5}_{-1.0}$ | $13.2^{+0.7}_{-0.2}$ | 40.5 |

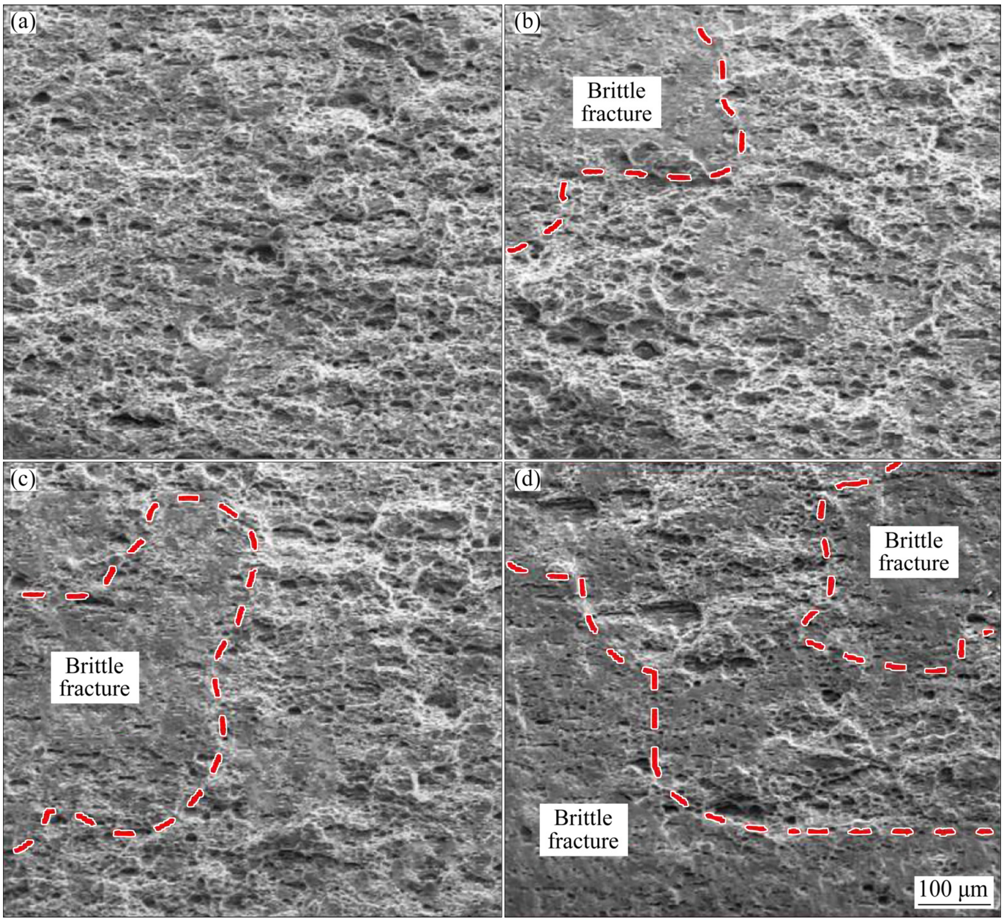


**Fig. 9** SEM fracture morphologies of samples tested in 3.5 wt.% NaCl solution: (a) Sample 1; (b) Sample 2; (c) Sample 3; (d) Sample 4

Therefore, studying the growth of SCC cracks could lead to a better understanding on the role of grain size in the SCC process. Figure 10 shows the SCC crack propagation path for Samples 1 and 4. Notably, Sample 1 exhibits a more tortuous crack propagation path with more deflections and crack closures. Crack branching along the crack path can also be observed in Fig. 10(a). Sample 1 has a microcrack and a crack width maintained <15 μm at the crack tip. In contrast, a relatively smooth and straight crack propagation path with no obvious deflections or crack closures is observed for Sample 4, as shown in Fig. 10(b). Its crack width reaches approximately 190 μm at the initial stage of cracking and gradually decreases along the crack propagation direction thereafter until reaching a crack tip width of 20−40 μm. In the study of the effect of 2524 Al alloy grain size on its fatigue crack growth behavior, SHOU et al [22] revealed that fatigue cracks propagated more tortuously in an alloy with grain sizes of 50–100 μm, whereas a smooth crack path with few closures was observed in an alloy with a grain size of 355.2 μm. MA et al [36] investigated the high-cycle fatigue and fatigue crack propagation characteristic of 5083-O Al alloy, noting that more tortuous fatigue crack propagation paths exhibit better fatigue properties. Similar results are obtained in this study. Therefore, samples with fine grains limit the crack propagation process, thereby exhibiting better SCC resistance.

To determine the relationship between the cracking mechanisms and grain structures, the short cracks (red boxes in Fig. 10) of the failed samples were observed by EBSD. Their SCC behavior is shown in Figs. 11(a, b). The main cracking mode of Sample 1, which has a fine grain structure, is intergranular cracking (Fig. 11(a)), while that of Sample 4, which has a coarse grain structure, is transgranular cracking (Fig. 11(b)). The grain orientation in the vicinity of the crack was also investigated, as shown in Figs. 11(a, b). The results show that the crack exhibits a distinct deflection at Grains 1, 2, 5, and 6 (close to the {011} orientation). However, a relatively smooth and straight crack propagation path without any obvious deflections is observed at Grains 3, 4, 5, 7, 8, and 9 (close to the {001} orientation). Therefore, the SCC cracks tend to pass through the {001} orientation grains, while the crack is prone to deflection upon encountering {011} orientation grains. This is in good agreement with the results of previous studies [37]. The results indicate that the {011} orientation grains may hinder crack propagation. Moreover, Figs. 11(c, d) present the GB distribution maps of the crack propagation regions in two samples. Here, the blue and red lines denote the HAGBs (>15°) and LAGBs (2°−15°), respectively. These results show that the number of LAGBs around the crack region is larger than that of HAGBs. The direction of crack propagation is orientated toward the LAGB region

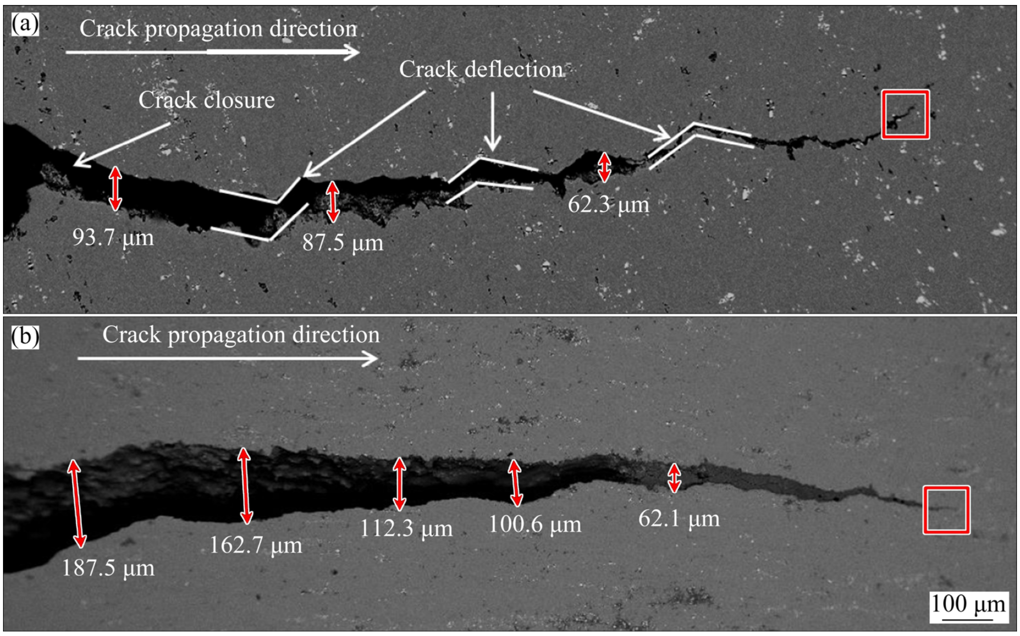


**Fig. 10** SCC crack propagation paths of Samples 1 (a) and 4 (b)

in the case of Sample 1, which is mainly attributed to its greater deformation degree caused by higher ductility than Sample 4. CHI et al [38] noted the crack propagation due to the impact toughness testing of Ti−Al−V−Mo−Zr alloy, in which they found that the direction of the crack propagation was orientated toward the LAGB region.

The cracking mechanisms of Samples 1 and 4 are obviously different. A model is proposed to explain the effect of the grain structure on the SCC resistance, as shown in Fig. 12. An electrochemical reaction is generated during SSRT in NaCl solution on the surfaces of the 5083 Al alloy. The oxidation reaction of Al ($Al \rightarrow Al^{3+}+3e$) resulted in the formation of $Al^{3+}$, with anodic dissolution [29]. The reduction reaction of $O_2+2H_2O+4e \rightarrow 4OH^-$ occurred at the cathode [39]. Simultaneously, due to the anode activity of the Mg−Si phase ($Mg_2Si+2H_2O \rightarrow 2Mg^{2+}+SiO_2+4H^++8e$), the electrochemical dissolution in the $Mg_2Si$ intermetallic compound will generate $H^+$. CHEN et al [40] reported that the presence of $Cl^-$ in an aqueous solution could promote the corrosion of alloys with an increased $Cl^-$ concentration, further accelerating the corrosion

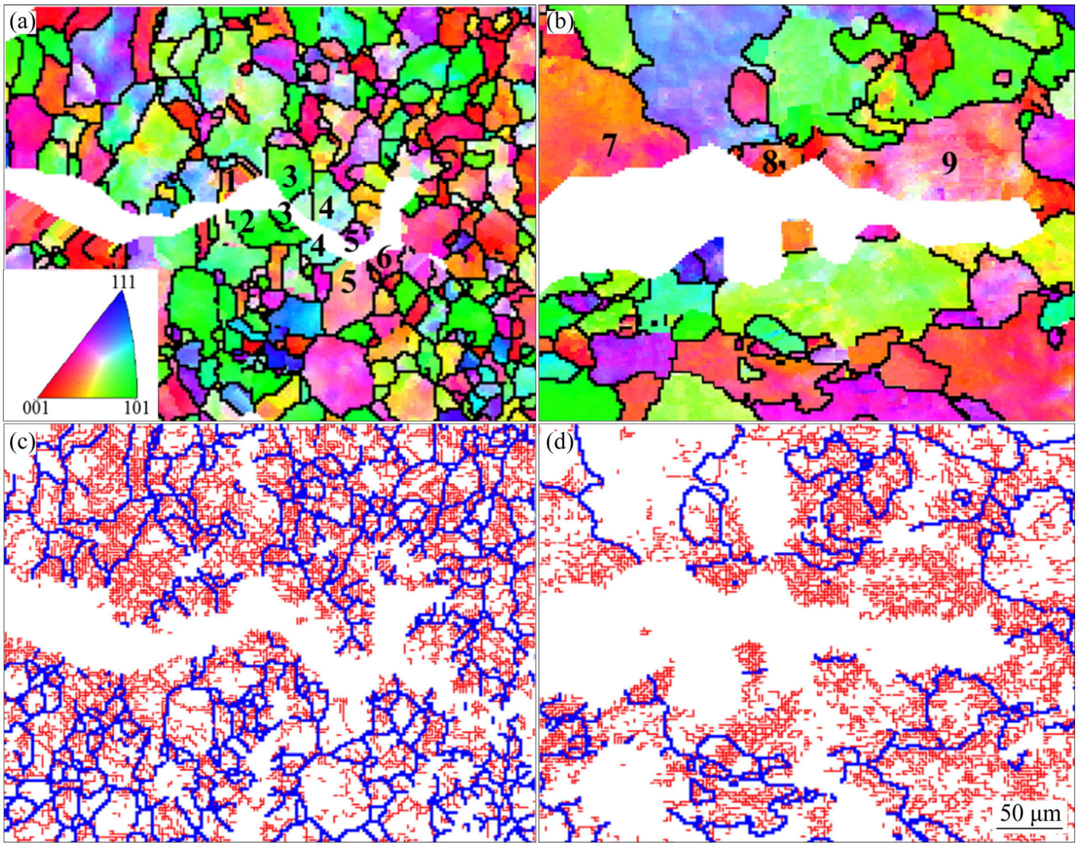


**Fig. 11** EBSD maps (a, b) and GB distributions (c, d) for SCC behavior of short crack in Sample 1 (a, c) [4], and Sample 4 (b, d)

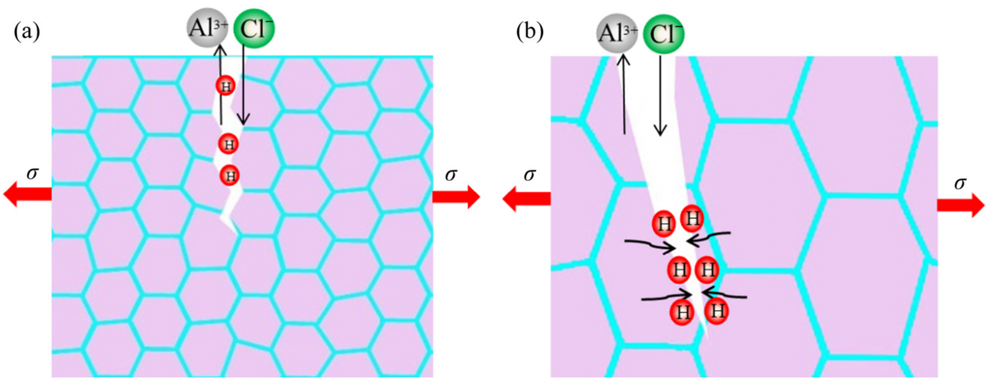


**Fig. 12** Schematic diagrams of samples with different grain structures during SCC process: (a) Sample 1; (b) Sample 4

rates. For Sample 4, the crack propagation mechanism is dominated by ion transport [41,42]. When the crack propagates along a relatively smooth path, $H^+$ and $Cl^-$ consistently fill the entire crack and are adsorbed onto the crack surface (Fig. 12(b)), thereby reducing the surface energy. Ion transport through the interior of a coarse grain could occur much more easily than in a fine grain, resulting in the typical transgranular cracking feature shown in Fig. 11(b). Moreover, the driving force is more concentrated at the crack tip under tensile stress, thereby accelerating crack propagation.

Grain refinement can improve the SCC resistance by increasing the number of GBs during the SCC propagation process. As a barrier, GBs could decrease the growth rate of SCC cracks and alter its growth path [11]. Due to the precipitation of the *β*-phase on the GBs, 5083 Al alloy has a tortuous propagation path of the corrosion crack [43]. So, the SCC mode has the typical characteristics of intergranular cracking, as shown in Fig. 11(a). When a crack propagates along a relatively tortuous path in fine grains, $H^+$ and $Cl^-$ can accumulate at the crack deflections (Fig. 12(a)). In this case, the crack slowly propagates due to the tortuous corrosion path and low $H^+$ and $Cl^-$ concentration. Moreover, since Sample 1 has an intergranular SCC cracking, cracks branch out when they encounter GBs with triple junctions. A triple junction is likely to have a low misorientation energy, thereby requiring a high crack tip driving force or ions concentration to achieve GBs decohesion [26], resulting in the relatively high SCC resistance of Sample 1. When a crack is deflected, the change in loading mode could influence the driving force for further crack propagation. Therefore, Sample 1, which has fine grains, exhibits better resistance to stress corrosion.

## 4 Conclusions

(1) The sample of fine grains (8.7 μm) shows worse IGC resistance with corrosion depth of 36 μm. Sample of coarse grains (79.2 μm) shows better IGC resistance with corrosion depth of 15 μm.

(2) The SSRT test demonstrated that fine grains exhibit better SCC resistance with an $I_{SSRT}$ of 11.2% than coarse grains with an $I_{SSRT}$ of 40.5%.

(3) Grain refinement can improve the SCC resistance by increasing the number of GBs, such that any corrosion crack propagation follows a tortuous path. The grains with a {011} orientation may hinder crack propagation and orientate the cracks toward the LAGB region.

(4) Slow crack propagation occurs in the sample with fine grains due to the tortuous corrosion path, and low $H^+$ and $Cl^-$ concentrations. In contrast, the crack propagation follows a relatively smooth path in the sample with coarse grains due to the adsorption of $H^+$ and $Cl^-$ onto the entire crack surface, thereby reducing the surface energy.

## Acknowledgments

The authors thank Dr. ZHANG for providing language polishing and assistance for the experiments. The authors also thank Henan Mingtai Aluminum Co., Ltd., China, for providing the test equipment, financial support and Program of the Ministry of Education in China (2011).

## References

[1] SAESSI M, ALIZADEH A, ABDOLLAHI A. Wear behavior and dry sliding tribological properties of ultra-fine grained Al5083 alloy and boron carbide-reinforced Al5083-based composite at room and elevated temperatures [J]. Transactions of Nonferrous Metals Society of China, 2021, 31: 74−91.

[2] ZHANG Zhi-chao, LIU Fu-chun, HAN En-hou, XU Long. Mechanical and corrosion properties in 3.5% NaCl solution of cold sprayed Al-based coatings [J]. Surface and Coatings Technology, 2020, 385: 125372.

[3] LENG Wen-bing, YUAN Ge-cheng, LU Hao-dong. Stress corrosion cracking behavior of 5083 aluminum alloy in SSRT [J]. Corrosion & Protection, 2009, 30(11): 794−796.

[4] LI Zhi, YI Dan-qing, TAN Cheng-yu, WANG Bin. Investigation of the stress corrosion cracking behavior in annealed 5083 aluminum alloy sheets with different texture types [J]. Journal of Alloys and Compounds, 2020, 817: 152690.

[5] MENG Chun-yan, ZHANG Di, ZHUANG Lin-zhong, ZHANG Ji-shan. Correlations between stress corrosion cracking, grain boundary precipitates and Zn content of Al−Mg−Zn alloys [J]. Journal of Alloys and Compounds. 2016, 655: 178−187.

[6] ZHAO Jing-wei, LUO Bing-hui, HE Ke-jian, BAI Zhen-hai, LI Bin, CHEN Wei. Effects of minor Zn content on microstructure and corrosion properties of Al−Mg alloy [J]. Journal of Central South University, 2016, 23(12): 3051−3059.

[7] FAN Le-tian, MA Ji-jun, ZOU Cheng-xiong, GAO Jun,

WANG Hai-sheng, SUN Jing, GUAN Quan-mei, WANG Jun, TANG Bin, LI Jin-shan, WANG William-yi. Revealing foundations of the intergranular corrosion of 5XXX and 6XXX Al alloys [J]. Materials Letters, 2020, 271: 127767.

[8] DING Yu-sheng, GAO Kun-yuan, HUANG Hui, WEN Sheng-ping, WU Xiao-lan, NIE Zuo-ren, GUO Shan-shan, SHAO Rui, HUANG Cheng, ZHOU De-jing. Nucleation and evolution of $\beta$ phase and corresponding intergranular corrosion transition at 100−230 °C in 5083 alloy containing Er and Zr [J]. Materials & Design, 2019, 174: 107778.

[9] MA Qi-biao, ZHANG Di, ZHUANG Lin-zhong, ZHANG Ji-shan. Intergranular corrosion resistance of Zn modified 5××× series Al alloy during retrogression and re-aging treatment [J]. Materials Characterization, 2018, 144: 264−273.

[10] SINGH D, JAYAGANTHAN R, NAGESWARA RAO P, KUMAR A, VENKETESWARLU D. Effect of initial grain size on microstructure and mechanical behavior of cryorolled AA 5083 [J]. Materials Today: Proceedings, 2017, 4(8): 7609−7617.

[11] HUANG Li-ying, WANG Kuai-she, WANG Wen, YUAN Jie, QIAO Ke, YANG Tao, PENG Pai, LI Tian-qi. Effects of grain size and texture on stress corrosion cracking of friction stir processed AZ80 magnesium alloy [J]. Engineering Failure Analysis, 2018, 92: 392−404.

[12] SUN Zhong-zhi, WANG Rui-yang, MEI Yu. Effect of grain size on stress corrosion cracking behavior of LY12 alloy [J]. Materials China, 2013, 32(3): 179−184.

[13] TSAI T C, CHUANG T H. Role of grain size on the stress corrosion cracking of 7475 aluminum alloys [J]. Materials Science and Engineering A, 1997, 225: 135−144.

[14] ARGADE G R, KUMAR N, MISHRA R S. Stress corrosion cracking susceptibility of ultrafine grained Al−Mg−Sc alloy [J]. Materials Science and Engineering A, 2013, 565: 80−89.

[15] OSÓRIO W, FREIRE C, GARCIA A. The role of macrostructural morphology and grain size on the corrosion resistance of Zn and Al castings [J]. Materials Science and Engineering A, 2005, 402: 22−32.

[16] MAHMOUD T S. Effect of friction stir processing on electrical conductivity and corrosion resistance of AA6063-T6 Al alloy [J]. Proceedings of the Institution of Mechanical Engineers, Part C: Journal of Mechanical Engineering Science, 2008, 222: 1117−1123.

[17] LIN Shuang-ping, NIE Zuo-ren, HUANG Hui, LI Bo-long. Annealing behavior of a modified 5083 aluminum alloy [J]. Materials & Design, 2010, 31: 1607−1612.

[18] LUO Bing-hui, DAN Yi-min, BO Zhen-hai. Effect of annealing temperature on microstructure and corrosive properties of cold-rolled 5083 aluminum alloy after quenching [J]. Journal of Central South University (Science and Technology), 2007(5): 802−808. (in Chinese)

[19] ZHANG Jia-yi, WANG Bin, YI Dan-qing. Stress corrosion cracking behavior in 2297 Al−Cu−Li alloy at different grain orientations [J]. Materials Science and Engineering A, 2019, 764: 138252.

[20] HE Wei-jun, CHEN Xin, LIU Na, LUAN Bai-feng, YUAN Gai-huan, LIU Qing. Cryo-rolling enhanced inhomogeneous deformation and recrystallization grain growth of a zirconium alloy [J]. Journal of Alloys and Compounds, 2017, 699: 160−169.

[21] NAH J J, KANG H G, HUH M Y, ENGLER O. Effect of strain states during cold rolling on the recrystallized grain size in an aluminum alloy [J]. Scripta Materialia, 2008, 58: 500−503.

[22] SHOU W B, YI D Q, LIU H Q, TANG C, SHEN F H, WANG B. Effect of grain size on the fatigue crack growth behavior of 2524-T3 aluminum alloy [J]. Archives of Civil and Mechanical Engineering, 2016, 16: 304−312.

[23] ENGLER O, MILLER-JUPP S. Control of second-phase particles in the Al−Mg−Mn alloy AA 5083 [J]. Journal of Alloys and Compounds, 2016, 689: 998−1010.

[24] ZHAO Yi-fu, POLYAKOV M, MECKLENBURG M, KASSNER M, HODGE A. The role of grain boundary plane orientation in the $\beta$ phase precipitation of an Al−Mg alloy [J]. Scripta Materialia, 2014, 89: 49−52.

[25] ARAFIN M A, SZPUNAR J A. A new understanding of intergranular stress corrosion cracking resistance of pipeline steel through grain boundary character and crystallographic texture studies [J]. Corrosion Science, 2009, 51: 119−128.

[26] WANG B J, XU D K, SUN J, HAN En-hou. Effect of grain structure on the stress corrosion cracking (SCC) behavior of an as-extruded Mg−Zn−Zr alloy [J]. Corrosion Science, 2019, 157: 347−356.

[27] LIU X Y, ADAMS J B. Grain-boundary segregation in Al−10%Mg alloys at hot working temperatures [J]. Acta Materialia. 1998, 46: 3467−3476.

[28] RALSTON K D, BIRBILIS N, DAVIES C. Revealing the relationship between grain size and corrosion rate of metals [J]. Scripta Materialia, 2010, 63: 1201−1204.

[29] YASAKAU K, ZHELUDKEVICH M, LAMAKA S, FERREIRA M. Role of intermetallic phases in localized corrosion of AA5083 [J]. Electrochimica Acta, 2007, 52: 7651−7659.

[30] CUI Qiang, YI Dan-qing, WANG Hong-xuan, ZHANG Jia-yi, XU Jiao, WANG Bin. Effects of grain size and secondary phase on corrosion behavior and electrochemical performance of Mg−3Al−5Pb−1Ga−Y sacrificial anode [J]. Journal of Rare Earths, 2019, 37: 1341−1350.

[31] SEARLES J L, GOUMA P I, BUCHHEIT R G. Stress corrosion cracking of sensitized AA5083 (Al−4.5Mg−1.0Mn) [J]. Metallurgical and Materials Transactions A, 2001, 32: 2859−2867.

[32] ZHU Zhi-xiong, JIANG Xing-xu, WEI Gang, FANG Xiao-gang, ZHONG Zhi-hong, SONG Kui-jing, HAN Jian, JIANG Zheng-yi. Influence of Zn content on microstructures, mechanical properties and stress corrosion behavior of AA5083 aluminum alloy [J]. Acta Metallurgica Sinica (English Letters), 2020, 33: 1369−1378.

[33] SHE Xin-wei, JIANG Xian-quan, WANG Pu-quan, TANG Bin-bin, CHEN Kang, LIU Yu-jie, CAO Wei-nan. Relationship between microstructure and mechanical properties of 5083 aluminum alloy thick plate [J]. Transactions of Nonferrous Metals Society of China, 2017, 682: 613−621.

[34] SHARMA M, ZIEMIAN C. Pitting and stress corrosion cracking susceptibility of nanostructured Al−Mg alloys in natural and artificial environments [J]. Journal of Materials

Engineering and Performance, 2008, 17: 870−878.
[35] LENG Wen-bing, LUO Ming-qiang, CHEN Shu-qin. A comparative study on stress corrosion cracking behavior of 5083 and 5A30 aluminum alloys [J]. Light Alloy Fabrication Technology, 2015, 43: 45−49.
[36] MA Ming-yang, ZHANG Jia-yi, YI Dan-qing, WANG Bin. Investigation of high-cycle fatigue and fatigue crack propagation characteristic in 5083-O aluminum alloy [J]. International Journal of Fatigue, 2019, 126: 357−368.
[37] MASOUMI M, SANTOS L, BASTOS I, TAVARES S, DA SILVA M, de ABREU H. Texture and grain boundary study in high strength Fe−18Ni−Co steel related to hydrogen embrittlement [J]. Materials & Design, 2016, 91: 90−97.
[38] CHI Guang-fang, YI Dan-qing, JIANG Bo, YANG Ling-yun, LIU Hui-qun. Crack propagation during Charpy impact toughness testing of Ti−Al−V−Mo−Zr alloy tubes containing equiaxed and lamellar microstructures [J]. Journal of Alloys and Compounds, 2021, 852: 156581.
[39] KIM Seong-jong, HAN Min-su, KIM Seong-kweon, JANG Seok-ki. Improvement of hydrogen embrittlement and stress corrosion cracking by annealing for Al−4.4Mg−0.6Mn alloy [J]. Transactions of Nonferrous Metals Society of China, 2011, 21: s17−s22.
[40] CHEN Jian, WANG Jian-qiu, HAN En-hou, DONG Jun-hua, KE Wei. AC impedance spectroscopy study of the corrosion behavior of an AZ91 magnesium alloy in 0.1M sodium sulfate solution [J]. Electrochimica Acta, 2007, 52: 3299−3309.
[41] CASAJÚS P, WINZER N. Intergranular stress corrosion crack propagation in hot-rolled AZ31 Mg alloy sheet [J]. Materials Science and Engineering A, 2014, 602: 58−67.
[42] YUAN Ding-ling, CHEN Song-yi, CHEN Kang-hua, HUANG Lan-ping, CHANG Jiang-yu, ZHOU Liang, DING Yun-feng. Correlations among stress corrosion cracking, grain-boundary microchemistry, and Zn content in high Zn-containing Al−Zn−Mg−Cu alloys [J]. Transactions of Nonferrous Metals Society of China, 2021, 31: 2220−2231.
[43] LIU Meng. Comparison of corrosion resistance for 5083 and 5059 aluminium alloy [J]. Ship Science and Technology, 2021, 43: 1−4. (in Chinese)

# 不同晶粒尺寸 5083 铝合金晶间腐蚀和应力腐蚀开裂的差异性

秦 晋[1,2]，李 志[3]，马明阳[1,2]，易丹青[1,2]，王 斌[1,2]

1. 中南大学 材料科学与工程学院，长沙 410083；
2. 中南大学 有色金属材料科学与工程教育部重点实验室，长沙 410083；
3. 中国民航局第二研究所，成都 610064

**摘 要**：通过冷轧和退火获得具有不同晶粒尺寸(8.7~79.2 μm)的 5083 铝合金板。研究其微观结构、晶间腐蚀(IGC)、应力腐蚀开裂(SCC) 和裂纹扩展行为。结果表明，粗晶粒样品表现出更好的抗 IGC 性能，其腐蚀深度为 15 μm。慢应变速率测试结果表明，细晶粒样品表现出更好的抗 SCC 性能，敏感性指数 $I_{SSRT}$ 为 11.2%。此外，基于裂纹扩展机制，晶粒细化可以通过增加晶界数量来诱导腐蚀裂纹沿曲折路径扩展，从而提高抗 SCC 性能；{011}取向的晶粒可以通过朝向小角度晶界区域阻碍裂纹扩展；曲折路径和低 $H^+$和 $Cl^-$浓度导致细晶材料中的裂纹扩展缓慢。

**关键词**：晶粒尺寸；晶间腐蚀；应力腐蚀开裂；裂纹扩展；5083 铝合金

**(Edited by Bing YANG)**